Global stability analysis for multidimensional flow using an augmented state vector formulation

By S. Lee, H. Song AND S. K. Lele

Global stability analysis is a powerful tool for predicting the onset of linear instabilities in complex flows, such as shock trains. However, its standard formulation as a differential eigenvalue problem tightly couples the flow physics with the numerical discretization, creating significant computational implementation challenges. This report presents an augmented state vector formulation that overcomes this limitation by redefining the state vector to include spatial derivatives as independent variables. This approach effectively transforms the governing equations into an algebraic system and separates the physical terms from the numerical scheme, enabling the flexible replacement of high-order methods for numerical differentiation according to the flow problems under consideration.

1. Introduction

With the improvement of computing power and algorithms, global stability analysis (GSA) has become a feasible tool for understanding the onset of linear instabilities in fluid flows that are inhomogeneous in more than one dimension, extending the classical linear stability analysis (LSA) approach, which applies to simple flows with only one-dimensional homogeneity such as parallel shear flows (Lin 1955; Drazin & Reid 2004) or axisymmetric vortical flows (e.g., Mao & Sherwin 2011; Lee & Marcus 2023). In inhomogeneous configurations, including flows over airfoils, or internal flows involving a series of shocks (or shock trains), one-dimensional stability formulations are no longer applicable. The instabilities in these systems are inherently global, meaning they are properties of the entire flow domain and cannot be understood by local solutions at specific wavenumbers (which mathematically assumes a spatial Fourier ansatz form). To avoid ambiguity with other uses of the term "global," the analyses of two- and three-dimensional base flows are often referred to as BiGlobal and TriGlobal analyses, respectively (Theofilis 2011). While GSA shares the concept of linearization with other linear analyses, it solves an eigenvalue problem (EVP) to identify self-sustained oscillatory modes, differing from resolvent analysis, which examines forcing-response amplification for prescribed real frequencies (e.g., McKeon & Sharma 2010).

The primary objective of GSA is to solve a large-scale, spatially multidimensional EVP to identify meaningful global modes. These modes typically represent the least stable coherent structures within the flow, and their characteristics—such as growth rate, oscillation frequency, and spatial structure—serve as a reasonable prediction for the initial transition from a steady to a time-dependent, often periodic, state. The successful application of GSA has provided profound physical insights into a wide array of fluid dynamics fields, such as aerospace engineering (e.g., Crouch *et al.* 2019) and geophysics (e.g., Chen *et al.* 2023).

The field of GSA has grown significantly in the three decades since the pioneering work of Pierrehumbert & Widnall (1982). As reviewed by Theofilis (2011), the scope of GSA has been extended to fluid engineering applications involving turbulence. Crouch *et al.*

(2007), for instance, applied GSA in a BiGlobal manner to a mean turbulent flow with the Spalart–Allmaras turbulence model, demonstrating that the origin of transonic airfoil buffeting is a linear global instability of the entire airfoil-shock system. This evolution has been enabled by ever-increasing computing power and the development of a variety of numerical methods, from early spectral methods to more flexible finite-difference, finite-volume, and finite-element approaches suitable for complex geometries.

At its core, one of the important computational challenges of GSA is solving a differential EVP that involves discretizing a matrix whose elements are themselves differential operators. This process creates a tight coupling between the physical coefficients of the base flow and the numerical differentiation scheme used for the spatial derivatives. The resulting implementation is rigid, making it difficult to modify or extend to a higher-order numerical method without a complete re-derivation of the discrete operators.

The new idea exposed in this report is state vector augmentation, which transforms the problem to segregate the analytic governing equations from the numerical discretization and differentiation scheme implementation. This is achieved through an augmented state vector formulation, where the state of the system is redefined to include not only the primitive flow variables but also their spatial derivatives as independent unknowns. By doing so, the differential operators in the governing equations are replaced by simple algebraic references to these new variables. This transforms the differential problem into a purely algebraic one and, crucially, separates the "physics" of the flow (encoded in one part of the final matrix) from the "numerics" of the discretization (encoded in another). This modularization offers a flexibility not possible with traditional methods.

The remainder of this report is structured as follows. Section 2 details the formulation of the augmented GSA framework, comparing it against the standard one to highlight its structural advantages. Section 3 presents a validation study using the canonical cases of incompressible Poiseuille flow and Taylor–Green vortices, demonstrating the framework's robustness and showcasing its inherent modularity by implementing and comparing different numerical schemes. Finally, Section 4 provides concluding remarks and outlines promising directions for future research and application of the method.

2. Fomulation of the augmented global stability analysis framework

2.1. *Standard linearized operator formulation*

Consider the two-dimensional Navier–Stokes equations as a representative example. The state variables are density ρ, velocity $\mathbf{u} = (u, v)$, and temperature T, which form the state vector $\mathbf{q} = (\rho, u, v, T)$. We decompose them into a known steady base flow $\overline{\mathbf{q}} = (\overline{\rho}, \overline{u}, \overline{v}, \overline{T})$ and a small unsteady perturbation $\mathbf{q}' = (\rho', u', v', T')$, i.e., $\mathbf{q}(x, y) = \overline{\mathbf{q}}(x, y) + \mathbf{q}'(x, y, t)$.

Substituting this decomposition into the governing equations (continuity, momentum, and energy) and only retaining linear perturbation terms yields a system of linear partial differential equations for the perturbation variables. For example, the linearized continuity, x-momentum, y-momentum, and energy equations are

$$\frac{\partial \rho'}{\partial t} + \frac{\partial(\overline{\rho}u' + \rho'\overline{u})}{\partial x} + \frac{\partial(\overline{\rho}v' + \rho'\overline{v})}{\partial y} = 0, \tag{2.1}$$

$$\begin{aligned} \frac{\partial(\overline{\rho}u' + \rho'\overline{u})}{\partial t} + \frac{\partial(\rho'\overline{u}^2 + 2\overline{\rho}\,\overline{u}u' + p')}{\partial x} + \frac{\partial(\overline{\rho}\,\overline{u}v' + \overline{\rho}u'\overline{v} + \rho'\overline{u}\,\overline{v})}{\partial y} \\ = \frac{\partial}{\partial x}(\tau'_{xx}) + \frac{\partial}{\partial y}(\tau'_{xy}), \end{aligned} \tag{2.2}$$

$$\frac{\partial(\overline{\rho}v' + \rho'\overline{v})}{\partial t} + \frac{\partial(\overline{\rho}\,\overline{u}v' + \overline{\rho}u'\overline{v} + \rho'\overline{u}\,\overline{v})}{\partial x} + \frac{\partial(\rho'\overline{v}^2 + 2\overline{\rho}\,\overline{v}v' + p')}{\partial y} = \frac{\partial}{\partial x}(\tau'_{xy}) + \frac{\partial}{\partial y}(\tau'_{yy}), \tag{2.3}$$

$$\frac{\partial(\rho'\overline{e} + \overline{\rho}e')}{\partial t} + \frac{\partial(\overline{u}(\overline{\rho}e' + \rho'\overline{e} + p') + u'(\overline{\rho}\,\overline{e} + \overline{p}))}{\partial x} + \frac{\partial(\overline{v}(\overline{\rho}e' + \rho'\overline{e} + p') + v'(\overline{\rho}\,\overline{e} + \overline{p}))}{\partial y} = \frac{\partial}{\partial x}(u'\overline{\tau}_{xx} + v'\overline{\tau}_{xy} + \overline{u}\tau'_{xx} + \overline{v}\tau'_{xy} + \phi'_x) + \frac{\partial}{\partial y}(u'\overline{\tau}_{xy} + v'\overline{\tau}_{yy} + \overline{u}\tau'_{xy} + \overline{v}\tau'_{yy} + \phi'_y), \tag{2.4}$$

where p is pressure, e is specific energy, and τ_{ij} is the shear stress tensor. For a Newtonian fluid with dynamic viscosity μ, its components are defined as $\tau_{xx} = 2\mu\,(\partial u/\partial x - (\nabla \cdot \mathbf{u})/3)$, $\tau_{yy} = 2\mu\,(\partial v/\partial y - (\nabla \cdot \mathbf{u})/3)$, and $\tau_{xy} = \mu\,(\partial u/\partial y + \partial v/\partial x)$. The heat flux vector, ϕ, has components $\phi_x = k\partial T/\partial x$ and $\phi_y = k\partial T/\partial y$, where k is the thermal conductivity. The system of equations can be specialized for different flow regimes. For compressible flows, the ideal gas law ($p = \rho RT$) is commonly used to close the system. Alternatively, for incompressible flows, ρ is assumed to be constant. In this case, p serves as the sole thermodynamic state variable, and the continuity and momentum equations decouple from the energy equation.

This system of linearized equations can be written in a compact operator form of

$$\frac{\partial}{\partial t}\mathcal{M}\mathbf{q}' + \mathcal{N}_{\overline{\mathbf{q}}}\mathbf{q}' = 0, \tag{2.5}$$

where $\mathcal{M}$ is a linear operator containing the time-derivative term coefficients, and $\mathcal{N}_{\overline{q}}$ is a linear spatial operator whose coefficients depend on the base flow $\overline{q}$. To search for temporally growing modes, a harmonic ansatz is introduced for the perturbation, i.e., $\mathbf{q}'(x, y, t) = \hat{\mathbf{q}}(x, y)e^{-i\omega t}$, where $\hat{\mathbf{q}}$ represents the global mode shape and ω is its complex frequency. This transforms the problem into a generalized EVP of

$$-i\omega\mathcal{M}\hat{\mathbf{q}} + \mathcal{N}_{\overline{\mathbf{q}}}\hat{\mathbf{q}} = 0. \tag{2.6}$$

This is typically converted to a standard EVP $\mathcal{L}\hat{\mathbf{q}} = i\omega\hat{\mathbf{q}}$, through a matrix transformation via $\mathcal{L} = \mathcal{M}^{-1} \circ \mathcal{N}_{\overline{\mathbf{q}}}$. The critical feature of this standard formulation is the structure of the operator $\mathcal{L}$. It is a 4×4 linear operator matrix whose elements are themselves differential operators. For example, a representative term from the transformed x-momentum equation operator is

$$\mathcal{L}_{22} = -\frac{\overline{u}}{\overline{\rho}}\left(\frac{\partial}{\partial x}\,(\overline{\rho}\,\cdot)\right) + \frac{1}{\overline{\rho}}\left[\frac{\partial}{\partial x}\,(2\overline{\rho}\,\overline{u}\,\cdot) + \frac{\partial}{\partial x}\,(\overline{\rho}\,\overline{v}\,\cdot) - \frac{\partial}{\partial x}\left(\frac{4\mu}{3}\frac{\partial}{\partial x}\right) - \frac{\partial}{\partial y}\left(\mu\frac{\partial}{\partial y}\right)\right]. \tag{2.7}$$

Eq. (2.7) explicitly exhibits the intimate coupling between physical coefficient terms (e.g., $\overline{u}$, $\overline{v}$, $\overline{\rho}$, μ) and spatial differential operators ($\partial/\partial x$, $\partial^2/\partial x^2$, $\partial/\partial y$, and $\partial^2/\partial y^2$). When this operator is discretized, each term must be treated individually. For instance, implementing a second-order finite-difference scheme requires developing specific stencils for terms like $\overline{\rho}^{-1}\partial(2\overline{\rho}\,\overline{u}u')/\partial x$ and $\overline{\rho}^{-1}\partial(\overline{\rho}\,\overline{v}u')/\partial x$. This coupling makes the implementation rigid, meaning that changing the numerical scheme would necessitate a complete re-derivation and re-implementation of the discrete form of every single element in the operator matrix $\mathcal{L}$.

2.2. *State vector augmentation and system construction*

We propose the augmented state vector formulation of GSA, which fundamentally restructures the problem to break this rigid coupling. The core idea is to treat the spatial derivatives of the state variables as new, independent variables.

For the four-variable system described previously, the governing equations contain derivatives up to second order. The augmented state vector, $\mathbf{q}'_{\text{aug}}$, is therefore defined as a 24×1 vector that includes each of the four primary perturbation variables (ρ', u', v', T') followed by their first- and second-order spatial derivatives. The structure is

$$\mathbf{q}_{\text{aug}} = \left(\rho, \frac{\partial\rho}{\partial x}, \frac{\partial\rho}{\partial y}, \frac{\partial^2\rho}{\partial x^2}, \frac{\partial^2\rho}{\partial y^2}, \frac{\partial^2\rho}{\partial x\partial y}, u, \ \cdots\ , \frac{\partial^2 T}{\partial x\partial y}\right). \tag{2.8}$$

In practice, some derivatives, such as the second-order derivatives of ρ', may not appear in the system of equations and can be excluded to reduce the size of the system. However, for descriptive purposes, it is assumed here that all five first- and second-order spatial derivatives for each state variable are included. We denote the components of this vector as $q_{\text{aug},1}, q_{\text{aug},2}, \ldots, q_{\text{aug},24}$, where $q_{\text{aug},1} = \rho$, $q_{\text{aug},2} = \partial\rho/\partial x$, $\cdots$, with the pattern repeating for each primitive variable (e.g., $q_{\text{aug},7} = u$, $q_{\text{aug},8} = \partial u/\partial x$, $\cdots$). For notational simplicity, the subscript "aug" will be omitted hereinafter.

With this new state vector, Eqs. (2.1)–(2.4) are transformed into purely algebraic expressions. Consider the linearized continuity equation, which in its standard form contains derivatives of ρ', u', and v'. By substituting each derivative term with its corresponding component from the augmented vector, the equation becomes an algebraic relation. For instance, the full transformed linearized continuity equation is

$$-i\omega q'_1 + (\nabla\cdot\overline{\mathbf{u}})\, q'_1 + \overline{u}q'_2 + \overline{v}q'_3 + \frac{\partial\overline{\rho}}{\partial x}q'_7 + \overline{\rho}q'_8 + \frac{\partial\overline{\rho}}{\partial y}q'_{13} + \overline{\rho}q'_{14} = 0. \tag{2.9}$$

The equation is a linear algebraic equation relating several components of the augmented state vector. Each of the four governing equations is transformed similarly, yielding four algebraic equations that form the "physical" part of the final system matrix.

The resulting system of equations takes the following generalized EVP form, after applying the harmonic ansatz ($\mathbf{q}'(x,y,t) = \hat{\mathbf{q}}(x,y)e^{-i\omega t}$),

$$i\omega\mathcal{W}\hat{\mathbf{q}} = \left[\begin{array}{c|c|c|c} \text{continuity equation coefficient row}_{(1\times24)} & & & \\ \hline x\text{-momentum equation coefficient row}_{(1\times24)} & & & \\ \hline y\text{-momentum equation coefficient row}_{(1\times24)} & & & \\ \hline \text{energy equation coefficient row}_{(1\times24)} & & & \\ \hline \mathcal{D}_{(5\times6)} & \mathcal{D}_{(5\times6)} & \mathcal{D}_{(5\times6)} & \mathcal{D}_{(5\times6)} \end{array}\right]\hat{\mathbf{q}}, \tag{2.10}$$

where $\mathcal{W}$ is a 24×24 constant matrix whose entries are zero except for $\mathcal{W}_{1,1}$, $\mathcal{W}_{2,7}$, $\mathcal{W}_{3,13}$, and $\mathcal{W}_{4,19}$ (i.e., the entries corresponding to the state variables) being unity. $\mathcal{D}$ is a modularized constraint block matrix where the derivative relationships are separately collected, i.e.,

$$\mathcal{D} = \begin{bmatrix} \partial/\partial x & -1 & 0 & 0 & 0 & 0 \\ \partial/\partial y & 0 & -1 & 0 & 0 & 0 \\ 0 & \partial/\partial x & 0 & -1 & 0 & 0 \\ 0 & 0 & \partial/\partial y & 0 & -1 & 0 \\ 0 & 0 & \partial/\partial x & 0 & 0 & -1 \end{bmatrix}. \tag{2.11}$$

These 20 additional rows (for the four-variable system) ensure that the components of the augmented vector are mathematically consistent. This structure highlights two key advantages: only first-order derivatives appear in the constraint matrix $\mathcal{D}$, simplifying the numerical discretization, and the entire system is highly modular due to the block-diagonal nature of the constraint section.

This reformulation provides several profound advantages over the standard approach:

• Modularity: The upper block of the matrix corresponding to the governing equations contains only physical coefficients from the base flow (e.g., $\overline{\rho}, \overline{u}$), while the lower block corresponding to the constraints contains only the coefficients of the chosen numerical differentiation scheme. Therefore, in a programming context, a "physics module" can be developed to provide the coefficients for the governing equations based on any fluid model (laminar, RANS, etc.), while a separate "numerics module" can provide the discrete differentiation operators for the constraints.

• EVP Solver Compatibility: The final form results in a generalized EVP. This allows the direct application of existing linear algebra libraries such as ARPACK or PETSc to find the leading eigenvalues and eigenvectors.

• High-Order Accuracy: The framework makes the implementation of high-order numerical schemes highly straightforward. To switch from a simple central differencing scheme to a dense Fourier/Chebyshev spectral differentiation, one simply needs to populate the $\partial/\partial x$ and $\partial/\partial y$ terms in the constraint block with the chosen discrete operators. There is no need to re-derive the discretization for each term in the governing equations.

The primary trade-off of this approach is an increased memory usage. By expanding the state vector from 4 to 24 variables (per grid point), the total number of unknowns in the global system increases by a factor of six. The resulting global matrix, with dimensions of $(N_{\text{points}} \times 24)^2$, can become very large. However, this cost is mitigated by the matrix's structure; it is extremely sparse, and the constraint block $\mathcal{D}$ consists of a repeating pattern determined by the numerical stencil. This high degree of structure is well-suited for efficient assembly and the sparse matrix-vector products required by the iterative eigensolvers used for large-scale problems, which can benefit from parallel computing.

3. Examples

3.1. *Poiseuille flow*

To validate the augmented state vector framework, it is applied to one of the most fundamental and historically significant problems in hydrodynamic stability: the linear stability of incompressible plane Poiseuille flow, whose velocity profile is

$$\overline{\mathbf{u}}/U_0 = (1 - y^2)\hat{\mathbf{e}}_x \tag{3.1}$$

between two parallel plates $-h \leq y \leq h$, where U_0 is the centerline velocity magnitude and h is a half-height. Generally, U_0 and h are used as reference scales, leading to the timescale of h/U_0. This flow was the subject of early pioneering studies that led to the development of the classical stability theory for parallel shear flows (Drazin & Reid 2004). The governing equation for this flow can be analytically reduced to the fourth-order Orr–Sommerfeld equation for the streamfunction. The seminal 1971 work by Orszag (1971) established the critical Reynolds number ($Re = \rho U_0 h/\mu$) as $Re_c = 5772.22$, where a first unstable eigenmode appears ($\mathrm{Im}(\omega) < 0$) with the streamwise wavenumber of 1.02.

Although this canonical parallel flow is one-dimensional and does not necessarily require a global solver, the purpose of solving it here as a benchmark problem is to establish the foundational verification of the global framework under development. Successfully reproducing this benchmark confirms the basic functionality of the developed GSA code.

For the two-dimensional incompressible problem, the state vector consists of the primitive variables $\mathbf{q} = (p, u, v)$. The governing linearized Navier–Stokes equations involve first derivatives of pressure and second derivatives of velocity. Therefore, a suitable choice for the augmented state vector $\mathbf{q}_{\mathrm{aug}}$ is

$$\mathbf{q}_{\mathrm{aug}} = \left(p, \frac{\partial p}{\partial x}, \frac{\partial p}{\partial y}, u, \frac{\partial u}{\partial x}, \frac{\partial u}{\partial y}, \frac{\partial^2 u}{\partial x^2}, \frac{\partial^2 u}{\partial y^2}, v, \frac{\partial v}{\partial x}, \frac{\partial v}{\partial y}, \frac{\partial^2 v}{\partial x^2}, \frac{\partial^2 v}{\partial y^2} \right). \tag{3.2}$$

Using the components of this vector (denoted q_1 through q_{13}), the linearized incompressible Navier–Stokes equations are transformed into the algebraic form of

$$q_5' + q_{11}' = 0, \tag{3.3}$$

$$\frac{\partial \overline{u}}{\partial x} q_4' + \overline{u} q_5' + \frac{\partial \overline{u}}{\partial y} q_9' + \overline{v} q_6' + \frac{1}{\rho} q_2' - \frac{\mu}{\rho} q_7' - \frac{\mu}{\rho} q_8' = i\omega q_4', \tag{3.4}$$

$$\frac{\partial \overline{v}}{\partial x} q_4' + \overline{u} q_{10}' + \frac{\partial \overline{v}}{\partial y} q_9' + \overline{v} q_{11}' + \frac{1}{\rho} q_3' - \frac{\mu}{\rho} q_{12}' - \frac{\mu}{\rho} q_{13}' = i\omega q_9'. \tag{3.5}$$

Along with 10 derivative constraints, the complete system for each grid point has a dimension of 13×13. This ultimately forms a global matrix EVP of size $(N_x \times N_y \times 13)^2$, where N_x and N_y are the number of grid points in the streamwise and wall-normal directions, respectively. Finally, at grid points on the walls, the governing equation rows are replaced by the Dirichlet boundary conditions, $u' = v' = 0$.

For the system discretization, the computational domain is specified to capture the critical eigenmode identified by the Orr–Sommerfeld solution. The domain length in the streamwise direction is set to $L_x/h = 1.96\pi$, corresponding to the critical wavenumber of 1.02, while the wall-normal domain length is $L_y/h = 2$. The Reynolds number is fixed at the critical value, $Re = 5772.22$. It is important to note that although the domain length is chosen based on the known critical wavenumber, the resulting solutions are formally global modes and have no *a priori* knowledge of the wavenumber itself. The computational grid consists of $N_x = 21$ uniformly distributed points in the streamwise direction, for which periodic boundary conditions are assumed, and $N_y = 401$ non-uniformly distributed points in the wall-normal direction, where a tanh clustering function with a clustering parameter of $\beta = 1.5$ is used.

For the large-scale EVP solver, we employ the software package ARPACK with the shift-and-invert Arnoldi method. ARPACK has been a common choice in several GSA studies (e.g., Crouch *et al.* 2007; Nichols & Lele 2011).

The present GSA framework with the state vector augmentation is primarily validated through a direct comparison with the classical Orr–Sommerfeld solution at the critical

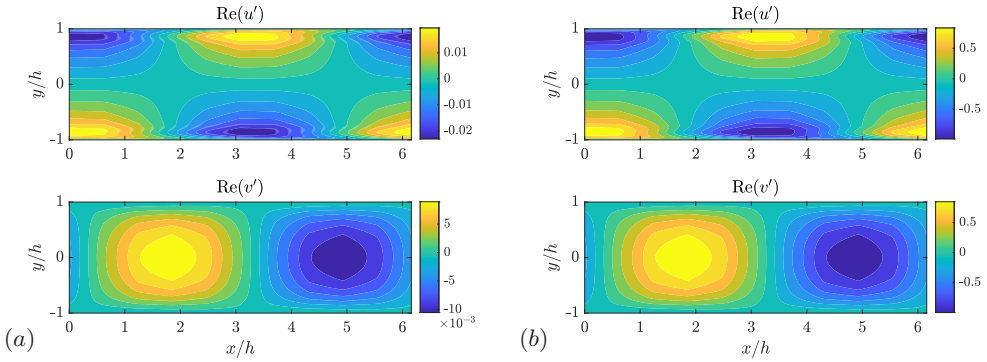

FIGURE 1. Comparison of the critical eigenmode velocity perturbation contours from (a) the present global stability analysis solver using a Fourier spectral differentiation in the x direction and a second-order central difference scheme in the y direction, and (b) from a 1D Orr–Sommerfeld equation solver.

Source	**Critical eigenvalue (ω_c)**
Orszag (1971)	0.2640 + 0.0000i
1D Orr–Sommerfeld solver (Chebfun)	0.2692 + 0.0000i
Global solver (present)	0.2696 + 0.0000i

TABLE 1. Comparison of the critical eigenvalue for plane Poiseuille flow at $Re = 5772.22$.

parameters. Figure 1 compares the least-stable eigenmode computed by the developed GSA solver (using a Fourier spectral differentiation for $\partial/\partial x$ and a second-order central difference for $\partial/\partial y$) with the solution from a 1D Orr–Sommerfeld solver (using the MATLAB Chebfun package).

The spatial structures of the global mode and the Orr–Sommerfeld mode are found to be identical. The resulting mode shape, with its anti-symmetric streamwise velocity perturbations strongest near the walls and symmetric wall-normal velocity perturbations peaked at the channel centerline, exhibits the classic footprint of a Tollmien–Schlichting (T-S) wave. This confirms that the global framework has correctly captured the primary physical instability mechanism for this flow. This is significant, as the global solver makes no *a priori* assumption about the perturbation's wavenumber (i.e., any multiple of $2\pi/L_x$ can appear as a wavenumber). In contrast, the solution from the Orr–Sommerfeld equation presumes a Fourier ansatz in the streamwise direction, $e^{i\alpha x}$, with the determined wavenumber of $\alpha = 1.02$. The fact that the global solver autonomously recovers this exact spatially periodic structure verifies the framework's robustness.

The accuracy of the global solver is quantified by comparing the computed eigenvalue with the established literature value from Orszag (1971) and the one-dimensional Orr–Sommerfeld solver result. As shown in Table 1, the eigenvalues are in close agreement. The computed eigenmode frequency (Re(ω)) from the global solver matches the benchmarks with high precision. The near-zero imaginary part (Im(ω)), which represents the exponential growth rate, correctly indicates that the critical state is slightly past the neu-

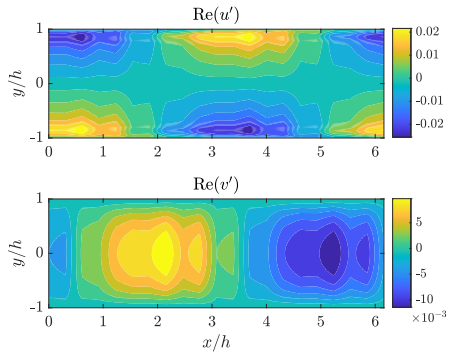

FIGURE 2. Leading eigenmode velocity perturbation contours from the present global stability analysis solver using a second-order central difference scheme for both spatial derivatives, leading to spurious oscillations.

tral stability boundary ($\mathrm{Im}(\omega) = 0$). This precise match further verifies the functionality and accuracy of the developed GSA framework.

Lastly, to demonstrate a key strength of the augmented state vector framework—the ease of numerical scheme replacement—the analysis was repeated using a second-order central difference scheme for both x and y spatial derivatives instead of the high-order spectral method. The resulting leading eigenmode is shown in Figure 2. The result from the lower-order scheme is contaminated with spurious, grid-scale oscillations (depicted as jagged contour lines). Such numerical artifacts are a well-known issue with low-order schemes, which struggle to accurately represent the smooth derivatives of the eigenfunction and can lead to undesirable numerical instability.

This comparison illustrates the advantage of the augmented state vector framework for GSA. Upgrading the solver from the inaccurate central difference scheme to the highly accurate spectral method was achieved simply by swapping the discrete differentiation matrices in the "numerics" part ($\mathcal{D}$ in Eq. (2.10)) of the global operator. This highlights the effortless modularity and flexibility of the augmented approach, which allows for the straightforward implementation of high-order accurate schemes.

3.2. *Taylor–Green vortices*

To further demonstrate the framework's capability, we apply it to the stability of two-dimensional Taylor–Green vortices. Unlike the parallel Poiseuille flow, which varies only in y, this base flow is genuinely multidimensional (varying in x and y), featuring a cellular array of counter-rotating vortices. The flow is defined by the stream function $\Phi(x, y)$, which is

$$\Phi(x, y) = \frac{A_0}{b_x^2 + b_y^2} \sin(b_x x) \sin(b_y y), \tag{3.6}$$

where $b_x = 2\pi/L_x$ and $b_y = 2\pi/L_y$ (L_x and L_y are the x and y periods of the flow, respectively) and A_0 is the maximum vorticity. This configuration is a classic benchmark for studying parametric instabilities, such as elliptic instability. We base our setup on the modal stability analysis performed by Gau & Hattori (2014), where the Reynolds number based on circulation in a single cell is $Re_\Gamma = \rho A_0 L_x L_y/(\pi^2 \mu) = 2500$. The cell aspect ratio is set to $L_x/L_y = 1.53$. The reference length scale is $L_x/2$, and the reference timescale is $4\pi/A_0$. Note that the time-invariant flow field expressed by Eq. (3.6) is a quasi-steady

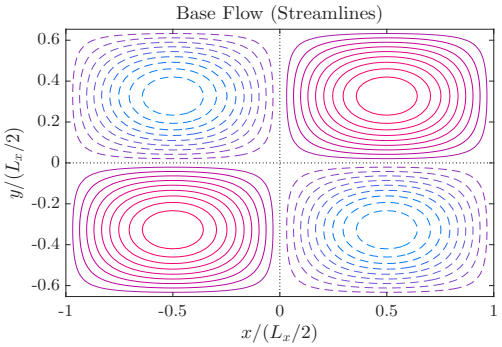

FIGURE 3. Streamlines of the Taylor–Green vortices, with two rotating clockwise (dashed lines) and two rotating counter-clockwise (solid lines).

solution of the incompressible Navier–Stokes equation (i.e., vorticity diffusion due to viscosity is marginal); we take this steady-state representation as the base flow.

For this problem, we analyze the three-dimensional stability of the two-dimensional base flow. The perturbation $\mathbf{q}'$ is assumed to take the form $\hat{\mathbf{q}}(x, y)e^{i(k_z z-\omega t)}$, where k_z is the axial wavenumber. This expands our primitive state vector to $\mathbf{q} = (p, u, v, w)$. Consequently, the augmented state vector $\mathbf{q}_{\text{aug}}$ grows to 18 components. This includes the 13 components for p, u and v and their x and y derivatives (as in the Poiseuille flow case), plus 5 new components for the axial velocity perturbation and its spatial derivatives: $w, \partial w/\partial x, \partial w/\partial y, \partial^2 w/\partial x^2$ and $\partial^2 w/\partial y^2$. The z derivative $\partial/\partial z$ in the governing equations is replaced by ik_z, while the derivatives in x and y are handled by the constraint matrix $\mathcal{D}$ as before. The resulting algebraic form, though larger, is structurally identical to the system of equations provided in Eqs. (3.3)–(3.5); its full derivation is straightforward and is omitted for brevity.

For the computational domain discretization, we use $N_x = N_y = 64$ uniformly distributed grid points. Fourier spectral differentiation is used for both $\partial/\partial x$ and $\partial/\partial y$ in the constraint matrix. This setup naturally imposes periodic boundary conditions, which corresponds to the "penetrating" case in Gau & Hattori (2014) and allows disturbances to induce transport between neighboring vortex cells. The non-dimensional domain size is 2.0 in the x direction (i.e., $L_x/(L_x/2)$) and is set to 1.3072 in the y direction (i.e., $L_y/(L_x/2)$), which yields the aspect ratio $L_x/L_y = 1.53$.

Our GSA solver is tested against the penetrating cases presented in Gau & Hattori (2014) (refer to p. 5), where the eigenmode structures and corresponding eigenvalues are provided. Figure 4 shows the z vorticity contours of these tested cases, which successfully replicate the results from Gau & Hattori (2014). The eigenvalue convention σ in Gau & Hattori (2014) is unclear; we found that using our $e^{-i\omega t}$ convention, our $\mathrm{Re}(\omega)$ corresponds to their $\mathrm{Im}(\sigma)$ and our $\mathrm{Im}(\omega)$ corresponds to their $-\mathrm{Re}(\sigma)$.

In Figure 4, the left panel (a) shows the eigenmode at a small axial wavenumber, $k_z = 0.62$. This is an oscillatory mode (i.e., non-zero $\mathrm{Re}(\omega)$) with vorticity concentrated near the hyperbolic stagnation points of the base flow. The right panel (b) shows the eigenmode at $k_z = 6.80$, which is non-oscillatory. The structure of this eigenmode is similar to that of bending waves, signified by the dipole-like perturbation structures found at each vortex center. This successful replication of these eigenmodes and their

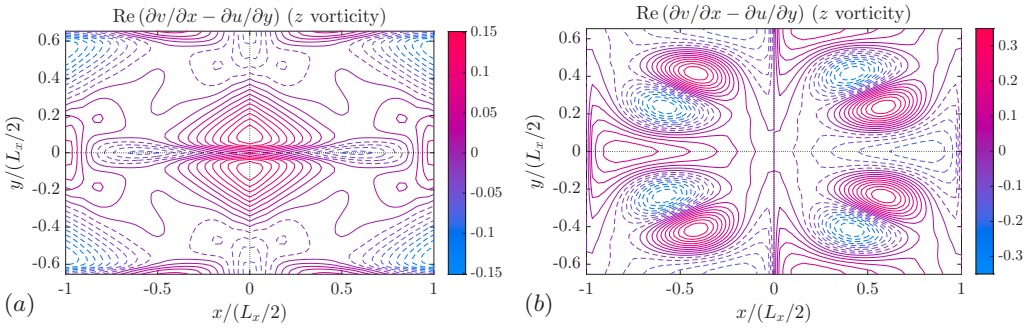

FIGURE 4. z vorticity contours of the eigenmodes of the Taylor–Green vortices (see Figure 3) obtained by the present solver, matching the structures reported from Gau & Hattori (2014, p. 5): (a) $k_z = 0.62$, $\omega = 3.069 - 0.748i$, (b) $k_z = 6.80$, $\omega = -1.170i$.

distinct structures further corroborates the robustness of the augmented GSA framework for genuinely multidimensional base flows.

4. Conclusion and future work

In this report, we elaborated on the augmented state vector formulation, a robust and flexible methodology for GSA. By transforming the governing differential eigenvalue problem into a standard algebraic one, the framework offers significant advantages. Its key strength lies in its modularity, which cleanly separates the physical model from the numerical scheme. This not only simplifies implementation by eliminating the need to directly discretize complex differential operators but also ensures compatibility with highly-optimized, parallelized linear algebra libraries. The validation with the stability analyses of Poiseuille flow and Taylor–Green vortices served as a verification of the developed GSA framework, confirming its accuracy and functionality for several promising future research directions.

The augmented GSA framework is planned to be extended to non-parallel flows in complex geometries with unstructured meshes, and further developed for full three-dimensional (i.e., TriGlobal) analysis of engineering configurations. A primary goal is to apply this framework to the study of shock trains in the isolators of high-speed scramjet engines (e.g., Morgan 2012). This problem is inherently three-dimensional, involving complex shock-wave/boundary-layer interactions that are strongly influenced by duct sidewalls and vary with the incoming Mach number. The stability of these shock trains is critical to engine performance, as instabilities can lead to undesirable oscillations or catastrophic engine unstart. The augmented framework is particularly well-suited for this TriGlobal analysis, which will allow for the investigation of complex compressible flow physics and the impact of geometric and flow parameters on stability. This extension to complex three-dimensional flows, including the application to turbulence closure models such as the Spalart-Allmaras RANS model (e.g., Crouch *et al.* 2007), represents the true potential of the proposed augmented GSA framework in engineering applications.

Acknowledgements

The support of ONR to CTR under grant N000142312833 is gratefully acknowledged.

REFERENCES

Chen, X., Gan, J. & McWilliams, J. C. 2023 BiGlobal analysis of baroclinic instability in a current-undercurrent oceanic system. *Phys. Rev. Fluids* **8**, 123801.

Crouch, J. D., Garbaruk, A. & Magidov, D. 2007 Predicting the onset of flow unsteadiness based on global instability. *J. Comp. Phys.* **224**, 924–940.

Crouch, J. D., Garbaruk, A. & Strelets, M. 2019 Global instability in the onset of transonic-wing buffet. *J. Fluid Mech.* **881**, 3–22.

Drazin, P. G. & Reid, W. H. 2004 *Hydrodynamic Stability*, 2nd ed. Cambridge University Press.

Gau, T. & Hattori, Y. 2014 Modal and non-modal stability of two-dimensional Taylor–Green vortices. *Fluid Dyn. Res.* **46**, 031410.

Lee, S. & Marcus, P. S. 2023 Linear stability analysis of wake vortices by a spectral method using mapped Legendre functions. *J. Fluid Mech.* **967**, A2.

Lin, C.-C. 1955 *The Theory of Hydrodynamic Stability*. Cambridge University Press.

Mao, X. & Sherwin, S. 2011 Continuous spectra of the Batchelor vortex. *J. Fluid Mech.* **681**, 1–23.

McKeon, B. J. & Sharma, A. S. 2010 A critical-layer framework for turbulent pipe flow. *J. Fluid Mech* **658**, 336–382.

Morgan, B. E. 2012 Large-eddy simulation of shock/turbulence interactions in hypersonic vehicle isolator systems. PhD thesis, Stanford University.

Nichols, J. W. & Lele, S. K. 2011 Global modes and transient response of a cold supersonic jet. *J. Fluid Mech.* **669**, 225–241.

Orszag, S. A. 1971 Accurate solution of the Orr–Sommerfeld stability equation. *J. Fluid Mech.* **50**, 689–703.

Pierrehumbert, R. T. & Widnall, S. E. 1982 The two- and three-dimensional instabilities of a spatially periodic shear layer. *J. Fluid Mech.* **114**, 59–82.

Theofilis, V. 2011 Global linear instability. *Annu. Rev. Fluid Mech.* **43**, 319–352.